APRIL 1997

FOM-INSTITUUT
VOOR
PLASMAFYSICA
RIJNHUIZEN

ASSOCIATIE
EURATOM-FOM

MHD STABILITY ANALYSIS of the KSTAR tokamak plasma

A.J.C. BELIËN, B. VAN DER HOLST, and J.P. GOEDBLOED

RIJNHUIZEN REPORT 97-232

FINAL REPORT ON KAERI KSTAR CONTRACT 96-428

This work was performed as part of the research programme of the association agreement of Euratom and the 'Stichting voor Fundamenteel Onderzoek der Materie' (FOM) with financial support from the 'Nederlandse Organisatie voor Wetenschappelijk Onderzoek' (NWO), Euratom, and the Korean Atomic Energy Research Institute (KAERI).

POSTBUS 1207
3430 BE NIEUWEGEIN
NEDERLAND
EDISONBAAN 14
3439 MN NIEUWEGEIN
TEL. 03402 - 31224
TELEFAX 03402 - 31204

Contents

1 Introduction **1**
1.1 Equilibrium 2

2 Ballooning stability analysis **5**
2.1 Summary of ballooning theory 5
2.2 Numerical solution 7
2.3 Optimized ballooning stable profiles 8
2.3.1 Scaling of optimized critical toroidal beta with plasma current 11
2.4 Shaping effects 11

3 Low-n stability analysis **23**
3.1 Introduction 23
3.2 Convergence properties of calculated low-n instabilities 23
3.3 Ideal instabilities 24
3.3.1 Internal modes 24
3.3.2 External modes 27
3.4 Resistive instabilities 29
3.5 Shaping effects 31

4 Conclusions **33**

A Ballooning stability code BSE, user guide version 1.3 **35**
A.1 Input files 35
A.2 Mapping file 37
A.3 Output 37
A.4 A remark on using BSE 38

Chapter 1

Introduction

This report concerns the magnetohydrodynamic (MHD) stability analysis of the South Korean KSTAR tokamak project, a follow-up of the KT-2 project [11]. At present the project is in the design phase. Table 1.1 contains the most up-to-date design parameters of the KSTAR tokamak relevant for MHD studies that were known at the time of writing.

Description	*symbol*	*value*
minor radius	a	0.5 m
major radius	R_0	1.8 m
inverse aspect ratio	ϵ	0.278
ellipticity	κ	2.0
triangularity	δ	0.8
magnetic field strength	B_0	3.15 T
Toroidal current	I_p	2 MA
normalized current	$\bar{I}$	1.596

Table 1.1: Parameters of the KSTAR tokamak.

The KSTAR tokamak is intended to be operated with a large, non-inductively driven bootstrap current. This bootstrap current is proportional to the pressure gradient and gives rise to off-axis peaked current densities and inverted q-profiles. Study of the stability tokamak equilibria with inverted q-profiles for KSTAR parameters is therefore the main subject of our stability studies.

Basically, our stability analysis splits into two parts, a study of ballooning and a study of global instabilities. In the first part, we investigate stability of KSTAR tokamak plasmas with respect to ballooning instabilities. As compared to the KT-2

tokamak design, KSTAR has a much more extreme elongation. Whereas the HBT code could be used for the computation of equilibria and ballooning stability of KT-2, this is no longer adequate for KSTAR since the conformal methods used in that code generate a disproportionate number of grid points near the equatorial plane. Therefore, a new state-of-the-art FORTRAN90 ballooning stability code was developed, called BSE (Ballooning Stable Equilibria). It requires input of an accurate equilibrium, such as provided by HELENA [8]. A user guide for BSE is provided in Appendix A.

In the second part of our stability study, instabilities with low toroidal mode numbers are studied. From previous studies, see for example Ref. [7] and references therein, it is known that infernal stabilities can put a limit on the maximum attainable plasma betas in plasma with inverted q-profiles. In this report, we discuss the ideal and resistive MHD analysis for low-n instabilities, for the profiles used in the ballooning section.

1.1 Equilibrium

For purpose of reference we here collect the basic quantities and equations describing the equilibrium as solved by HELENA.

From the cylindrical R,Z,ϕ coordinates, with the center of the plasma given by R_0 and the horizontal size by $2a$, convenient dimensionless coordinates are obtained:

$$x \equiv \frac{R - R_0}{a}, \qquad y \equiv \frac{Z}{a}. \tag{1.1}$$

The inverse aspect ratio is given by

$$\epsilon \equiv \frac{a}{R_0}, \tag{1.2}$$

a dimensionless flux label $0 \leq \psi \leq 1$ is obtained by dividing the poloidal flux by the total poloidal flux Ψ_1:

$$\psi \equiv \frac{\Psi}{\Psi_1}, \tag{1.3}$$

and an important parameter proportional to the value of the edge safety factor q_1 is given by

$$\alpha \equiv \frac{a^2 B_0}{\Psi_1}, \tag{1.4}$$

where B_0 is the value of the vacuum magnetic field at $R = R_0$.

Exploiting these parameters, the two arbitrary flux functions $p(\Psi)$ and $RB_\phi = F(\Psi)$ are replaced by dimensionless functions in terms of the flux label ψ:

$$P(\psi) \equiv \frac{\mu_0 \alpha^2}{\epsilon B_0^2} p(\Psi), \tag{1.5}$$

$$G(\psi) \equiv \frac{\alpha^2}{2a^2B_0^2}\left[F^2(\Psi) - R_0^2B_0^2\right] + \frac{\mu_0\alpha^2}{\epsilon^2B_0^2}p(\Psi). \tag{1.6}$$

In the Grad-Shafranov equation only their flux derivatives appear, which facilitates the introduction of the two unit profiles $\Gamma(\psi)$ and $\Pi(\psi)$ describing the freedom of the flux functions:

$$\frac{dG}{d\psi} = -A\Gamma(\psi), \qquad \frac{dP}{d\psi} = \frac{1}{2}AB\Pi(\psi). \tag{1.7}$$

The basic dimensionless equilibrium equation then takes the form

$$\psi_{xx} + \psi_{yy} - \frac{\epsilon}{1+\epsilon x}\psi_x = A\left[\Gamma(\psi) + Bx\left(1 + \frac{1}{2}\epsilon x\right)\Pi(\psi)\right], \tag{1.8}$$

which is to be solved subject to the boundary conditions $\psi = 1$ at the plasma boundary and $\psi = \psi_x = \psi_y = 0$ at the magnetic axis. This turns both A and B into eigenvalues, related to the physical parameters q_1 and β.

The cross-section of the plasma is prescribed by

$$x = a\cos(\gamma + \delta\sin\gamma), \tag{1.9}$$

$$y = b\sin\gamma, \tag{1.10}$$

where γ is an auxilary angle, $\kappa \equiv b/a$ is the ellipticity, and δ is the triangularity of the cross-section.

Important physical parameters are the poloidal beta:

$$\beta_{\rm p} \equiv \frac{8\pi S < p >}{\mu_0 I_{\rm p}^2}, \tag{1.11}$$

where S is the cross-sectional area, the toroidal beta:

$$\beta_{\rm t} \equiv \frac{2\mu_0 < p >}{B_0^2}, \tag{1.12}$$

and the edge safety factor:

$$q_1 \equiv f\frac{2\pi a^2 B_0}{\mu_0 R_0 I_{\rm p}}, \tag{1.13}$$

where f is an order of unity factor to be obtained from the equilibrium solution. The latter quantity is related to the normalized plasma current:

$$\bar{I} \equiv \frac{\mu_0 I_{\rm p}}{aB_0} \quad \rightarrow \quad q_1 = \frac{2\pi\epsilon f}{\bar{I}}. \tag{1.14}$$

In the Troyon scaling the so-called normalized beta appears:

$$\beta_{\rm N} = 100\frac{\beta_{\rm t}}{\bar{I}}. \tag{1.15}$$

Finally, the three parameters β_{p}, β_{t}, and q_1 exhibit the following important scaling relationship:

$$\epsilon\beta_{\mathrm{p}} = \left(\frac{\sigma}{f^2}\right)\frac{\beta_{\mathrm{t}}}{\epsilon}q_1^2, \tag{1.16}$$

where $\sigma \equiv S/(\pi a^2)$.

Chapter 2

Ballooning stability analysis

2.1 Summary of ballooning theory

At high beta, the most dangerous instabilities, in terms of limiting the maximum obtainable β, are usually characterized by highly localized perturbations. These instabilities, the ballooning modes [1], are driven by the pressure gradient p' and the curvature of the field lines, producing a negative potential energy on the outside of the tokamak.

The ballooning ordering is one where the wave vector $\mathbf{k}$ is large, but ω finite and $\mathbf{k}$ is constrained to be perpendicular to the total magnetic field $\mathbf{B}$ in all orders. For this ordering, the compression term in the potential energy δW of the perturbations is assumed to be small. Furthermore, up to second order, the kinking term proportional to the parallel current density vanishes. The remaining terms in δW describe a competition between the destabilizing effect of unfavorable curvature and the stabilizing effect of field line bending.

By choosing the poloidal ϑ such that the magnetic field lines become straight in the (ϑ, ϕ) plane, δW can be written as [6]

$$\delta W(\psi) = \int_{-\infty}^{\infty} \left[\frac{1}{R^2 B_p^2} \left(1 + \frac{k_n^2}{k_\pi^2}\right) \frac{1}{J} \left(\frac{\partial X}{\partial \vartheta}\right)^2 - \frac{2}{R B_p} \left(\kappa_n - \frac{k_n}{k_\pi} \kappa_g\right) p' X^2 \right] d\vartheta. \quad (2.1)$$

Here, B_p and B_ϕ are the poloidal and toroidal magnetic field, respectively, R is the major radius, and

$$J \equiv (\nabla\psi \times \nabla\vartheta \cdot \nabla\varphi)^{-1} = R\sqrt{g_{11} g_{22} - g_{12}^2} \quad (2.2)$$

is the Jacobian. The two components of the local wave vector are given by

$$k_n = -R B_p \left[q'(\vartheta - \vartheta_0) - (g_{12}/g_{22}) q \right], \quad (2.3)$$

$$k_\pi = -B/(RB_p), \tag{2.4}$$

where

$$q = IJ/R^2 = q(\psi) \tag{2.5}$$

is the safety factor. Furthermore,

$$\kappa_p = \frac{R}{J}\left(\partial_\psi - \partial_\vartheta \frac{g_{12}}{g_{22}}\right) JB_p, \tag{2.6}$$

$$\kappa_t = B_p\left(\partial_\psi - \frac{g_{12}}{g_{22}}\partial_\vartheta\right) R \tag{2.7}$$

are the poloidal and toroidal curvatures of the magnetic surfaces, respectively, and

$$\kappa_n = -\left(B_p^2/B^2\right)\kappa_p - \left(B_\varphi^2/B^2\right)\kappa_t, \tag{2.8}$$

$$\kappa_g = \frac{I}{JRB_pB^2}\frac{\partial B}{\partial \vartheta} \tag{2.9}$$

are the normal and geodesic curvature component of the magnetic field line curvature.

Eq. (2.1) is derived by the so-called ballooning transformation to an extended domain $-\infty < \vartheta < \infty$ of the poloidal angle, developed by Connor *et al.* [1]. This avoids the problem of the incompatibility of shear with poloidal periodicity. This way, the analysis of periodic eigenfunctions over the domain $0 < \vartheta < 2\pi$ is replaced by a summation over non-periodic "quasi-modes" in the extended domain. So, by introducing the ballooning transformation followed by the quasi-mode form decouples the stability analysis from surface to surface and provides a complete minimization of δW at large toroidal mode number n.

Minimization of δW leads to the Sturm-Liouville problem

$$-\frac{1}{J}\frac{\partial}{\partial\vartheta}\frac{1}{R^2B_p^2}\left(1+\frac{k_n^2}{k_\pi^2}\right)\frac{1}{J}\frac{\partial X}{\partial\vartheta} - \frac{2}{RB_p}\left(\kappa_n - \frac{k_n}{k_\pi}\kappa_g\right)p'X$$
$$= \rho\omega^2\frac{1}{R^2B_p^2}\left(1+\frac{k_n^2}{k_\pi^2}\right)X. \tag{2.10}$$

The value of ϑ_0 is determined by minimizing the potential energy with respect to ϑ_0:

$$\frac{\partial(\delta W)}{\partial\vartheta_0} = 0. \tag{2.11}$$

The resulting growth rate will have a maximum value then.

In practice, one is not interested in whether or not the plasma is stable, but one wants to exclude instabilities that grow faster than a certain small threshold growth rate. This leads to the concept of the σ-stability [4], where an equilibrium is called

σ-stable if no eigenvalues $\omega^2 < -\sigma^2$ exist, and σ-unstable if such eigenvalues do exist. The resulting modified potential energy for this case is

$$\delta W^\sigma(\psi) = \int_{-\infty}^{\infty} \left[P(\vartheta, \psi) \left(\frac{\partial X}{\partial \vartheta} \right)^2 + Q(\vartheta, \psi) X^2 \right] d\vartheta, \tag{2.12}$$

where

$$P(\vartheta, \psi) = \frac{1}{R^2 B_p^2} \left(1 + \frac{k_n^2}{k_\pi^2} \right) \frac{1}{J}, \tag{2.13}$$

$$Q(\vartheta, \psi) = -\frac{2J}{RB_p} \left(\kappa_n - \frac{k_n}{k_\pi} \kappa_g \right) p' + \sigma^2 \rho J^2 P. \tag{2.14}$$

Equation 2.12 is implemented in the ballooning stability code BSE.

2.2 Numerical solution

In most cases of ballooning analysis, one is interested in whether or not the equilibrium is σ-stable, i.e., one is only interested in the sign of the minimum of the modified potential energy δW^σ. In the BSE code, the Suydam method is implemented. This method is based on a finite difference scheme introduced by Suydam to calculate the marginal stability of an axisymmetric cylindrical plasma column [14]. The method can also be applied to ballooning analysis [3].

By replacing the variables in the energy functional Eq. (2.12) by their centered finite difference expressions, arranging the resulting terms for δW^σ to obtain squares, and truncating the extended domain to a finite one with N intervals, Eq. (2.12) can be rewritten as

$$\delta W^\sigma = \sum_{i=0}^{N} \alpha_i (Y_i)^2, \quad \alpha_0 = A_{0,0}, \quad \alpha_i = A_{i,i} - \frac{A_{i-1,i}^2}{\alpha_{i-1}}, \tag{2.15}$$

$$Y_i = X_i + \frac{A_{i,i+1}}{\alpha_i} X_{i+1}, \quad Y_N = X_N. \tag{2.16}$$

The tridiagonal matrix $A_{i,j}$ $(i, j = 0, \ldots N)$ is given by

$$A_{i,i} = \frac{1}{\Delta\vartheta} \left(P_{i-1/2} + P_{i+1/2} \right) + \frac{\Delta\vartheta}{4} \left(Q_{i-1/2} + Q_{i+1/2} \right), \tag{2.17}$$

$$A_{i+1,i} = A_{i,i+1} = -\frac{1}{\Delta\vartheta} P_{i+1/2} + \frac{\Delta\vartheta}{4} Q_{i+1/2}, \tag{2.18}$$

$$A_{i,j} = 0, \quad i \neq j-1, j, j+1, \tag{2.19}$$

with the initial condition

$$P_{-1/2} = Q_{-1/2} = 0, \tag{2.20}$$

where $\Delta\vartheta$ is the mesh size of the poloidal angle.

From Eq. (2.15) one can see that δW^{σ} is positive definite if and only if all the α_i's are positive. Thus, if one of the α_i's is negative the flux surface under consideration is ballooning σ-unstable. The resulting procedure is quite fast and converges rapidly, even when the mesh size $\Delta\vartheta$ is large or when the eigenfunction has a singularity inside the truncated interval. Note that when the ballooning mode is centered around $\vartheta_0 = 0$, we only need to integrate from $\vartheta = 0$ to ∞.

According to [3], the position ϑ_i where the α_i's become negative may be detected on an angular interval of the order of the decay length of the eigenfunction, i.e. of the order of the half-width of the eigenfunction. Furthermore, the growth rate always decreases as the marginal value ϑ_i increases. Thus, setting a maximum value on ϑ is equivalent with considering σ-stability, i.e., neglecting modes with very small growth rates. Finally, the marginal value of ϑ_i converges very fast with decreasing values of the mesh size $\Delta\vartheta$. Below a certain value of $\Delta\vartheta$, the value of ϑ_i remains practically constant.

2.3 Optimized ballooning stable profiles

In this section we calculate the ballooning stability properties for equilibria which resemble equilibria calculated by the transport code JETTO for typical reversed shear JET discharges. The considered profiles are the same as the ones used by Poedts *et al.* [11] in their stability study of KT-2 plasmas. The goal is to get a measure for the maximum attainable beta with respect to ballooning stability for such typical reversed shear equilibria.

The equilibrium is calculated with HELENA [8, 13] using 41 radial and 129 angular grid points. However, the angular resolution of metric coefficients in the mapping file, i.e. the information needed for CASTOR and BSE, is down sized to 65 angular grid points. No grid accumulation is used. The profiles $\Gamma(\psi)$ and $\Pi(\psi)$ are specified in HELENA through the `IGAM=4` and `IPAI=7` input switches by prescribing their values on 21 grid points evenly spaced in $\sqrt{\psi}$. These profiles are then mapped onto 41 grid points by interpolation. To do this we had to adapt HELENA since the original interpolation of the profiles assumed them to be specified on an equidistant mesh in ψ. In Fig. 2.1, the profiles Γ and Π are shown. For $\alpha = 1.93$ and $B = 2.5$, the flux coordinate grid calculated by HELENA is shown in Fig. 2.2.

The equilibrium corresponding to the considered profiles is ballooning unstable with growth rates greater than $0.1\,\tau_{\mathrm{A}}^{-1}$, where $\tau_{\mathrm{A}} \equiv R_{\mathrm{M}}\sqrt{\mu_0\rho_{\mathrm{M}}}/B_{\mathrm{M}}$, and R_{M} is the radius of the magnetic axis, and ρ_{M} and B_{M} are the magnitudes of the density and the magnetic field on axis. The unstable surfaces are located in the region of small positive shear. Since near the magnetic axis an additional extremum is present (although much less pronounced than the global minimum), there are also some unstable surfaces in the small positive shear region associated with this extremum position.

To stabilize the above equilibrium we fix Γ (which more or less fixes the current density profile) and locally decrease the pressure gradient. The following procedure

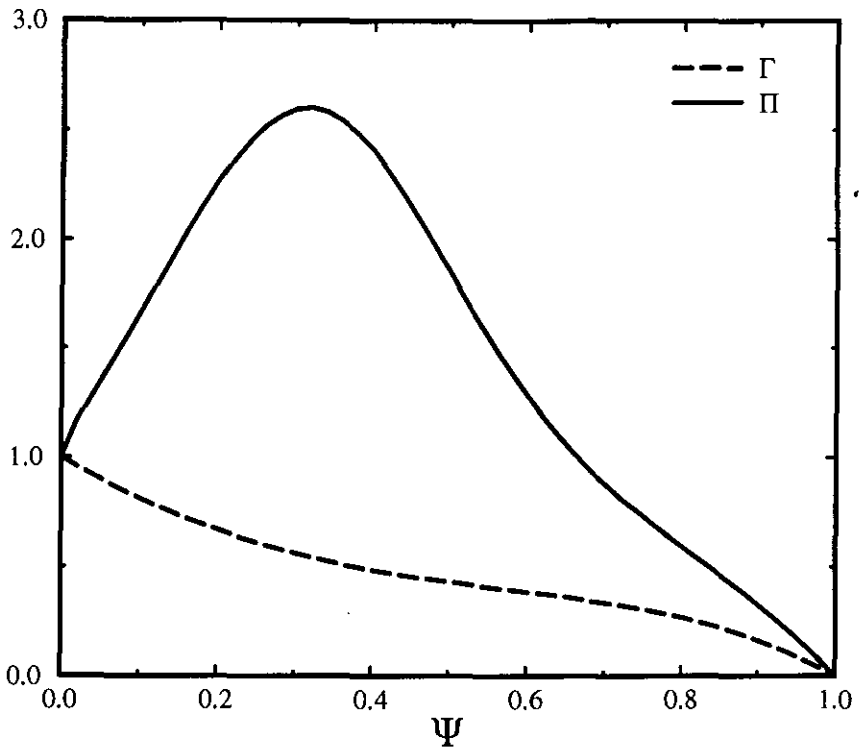

Figure 2.1: Γ and Π profiles exploited for the ballooning stability studies.

turned out to be the most efficient:

1. Start at the unstable flux surface ψ' located in the positive shear region closest to the $q_{\min}$ flux surface.
2. Decrease $\Pi(\psi')$ with 0.01 until the flux surface ψ' is ballooning stable.
3. Repeat steps 1–2 until all flux surfaces in the positive shear region are stabilized.
4. Perform steps 1–3, for the unstable surfaces (if present) in the small positive shear region near the axis.

The obtained pressure profile is *locally* marginally ballooning stable in the sense that an increase of Π with 0.01 at any of the surfaces that were initially unstable results in instability. An optimization is then performed by increasing the Shafranov shift (through the parameter B in HELENA) until the equilibrium is *globally* marginally ballooning stable.

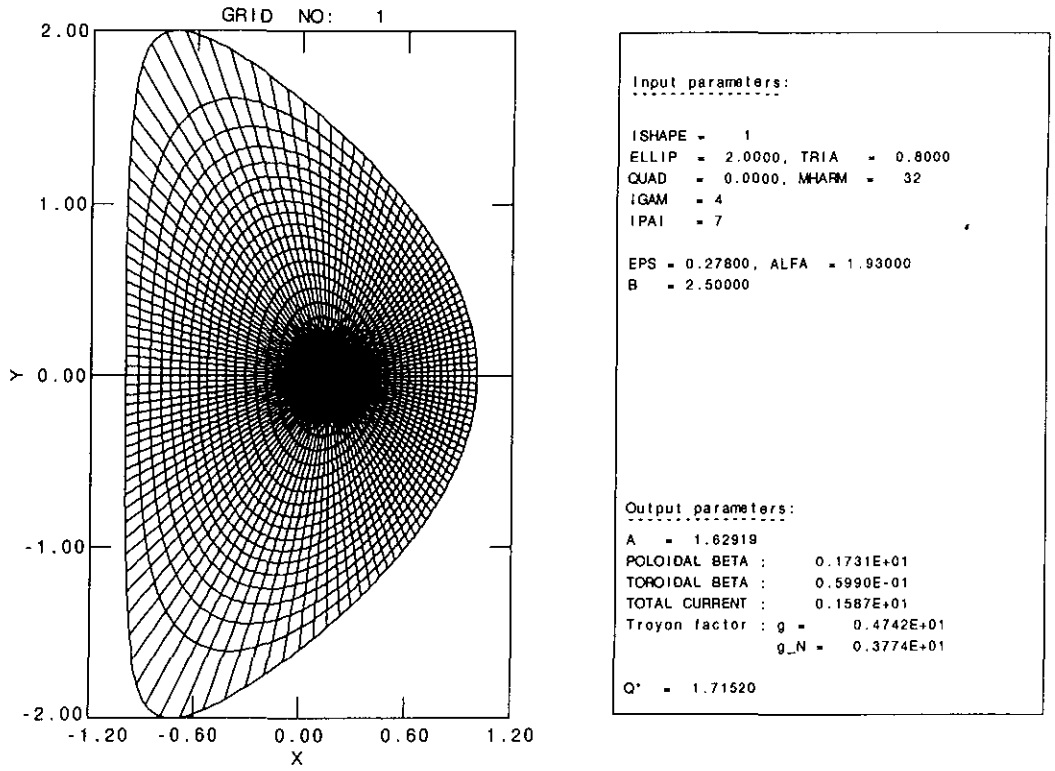

Figure 2.2: Straight field line coordinate grid and parameters for the equilibrium construction with HELENA (`ALFA=1.93, B=2.5, NR=41, NP=129, NRMAP=41, NPMAP=65`).

Figure 2.3 shows the pressure profiles, the averaged current density, and the q-profiles for three ballooning stable equilibria with different Shafranov shifts. It is clear that the current density and the q-profile are almost unaltered except for a small region near the axis. This shows that fixing the Γ profile is sufficient to keep the current density more or less constant. Equilibria B and C have small positive shear on axis which is favourable for stabilizing the pressure driven interchange instabilities. Equilibrium C is near *global* marginal ballooning stability in the sense that a tiny increase of the Shafranov shifts results in instability for almost all flux surfaces. The values of the input and output parameters for the three equilibria are listed in Tables 2.3 and 2.3.

Compared to KT-2 plasmas, it is clear that higher poloidal and toroidal plasma betas can be obtained. Assuming that the highest attainable stable beta for plasma with inverted shear scales linearly with the normalized plasma current $\bar{I}$, as found by Sykes *et al.* [15] for positive shear plasmas, the higher stable betas are due to a higher normalized plasma current ($\bar{I} = 0.838$ for KT-2 versus $\bar{I} = 1.596$ for KSTAR).

Eq.	$\bar{I}$	β_p	β_t	β_N	q_0	q_{min}	q_1	$\psi_{marginal}$
A	1.60	1.60	5.67	3.53	1.76	1.35	8.6	0.30–0.49
B	1.63	1.77	6.41	3.94	1.55	1.27	9.0	0.04–0.56
C	1.59	1.88	6.52	4.10	1.45	1.26	9.7	0.01–0.56

Table 2.1: Equilibrium parameters for the three ballooning stable equilibria A, B, and C. Equilibria A and B are locally marginal ballooning stable. Equilibrium C is near global marginal stability.

Eq.	ALFA	A	B
A	1.93	1.63	2.5
B	1.85	1.62	3.0
C	1.85	1.61	3.5

Table 2.2: HELENA parameters for the equilibria A, B, and C.

Notice, that the normalized β_N's also have relatively large values.

Although we used a fixed Γ-profile and performed an optimalization for the pressure only, ballooning stable equilibria with respect to the first region of stability with high values for the toroidal plasma beta were obtained. Even higher values for beta might be achieved by also optimizing the current density profiles.

2.3.1 Scaling of optimized critical toroidal beta with plasma current

In this subsection we investigate the scaling of the optimal critical toroidal plasma beta with the plasma current. We have done the calculations in the same way as described above, keeping the Γ-profile fixed and adjusting the pressure gradient locally, but with 257 poloidal grid points and 129 radial grid points. This was done to obtain better converged critical ballooning beta values.

The optimized beta values for three different values of the normalized plasma current are shown in Table 2.3. Since $\beta_N \approx 4$ for the different plasma currents considered and $\beta_t = \beta_N \bar{I}$, it follows that β_t scales linearly with the plasma current.

2.4 Shaping effects

In this section we consider shaping effects on ballooning stability. We vary the ellipticity, the triangularity, and the aspect ratio, and calculate the critical toroidal

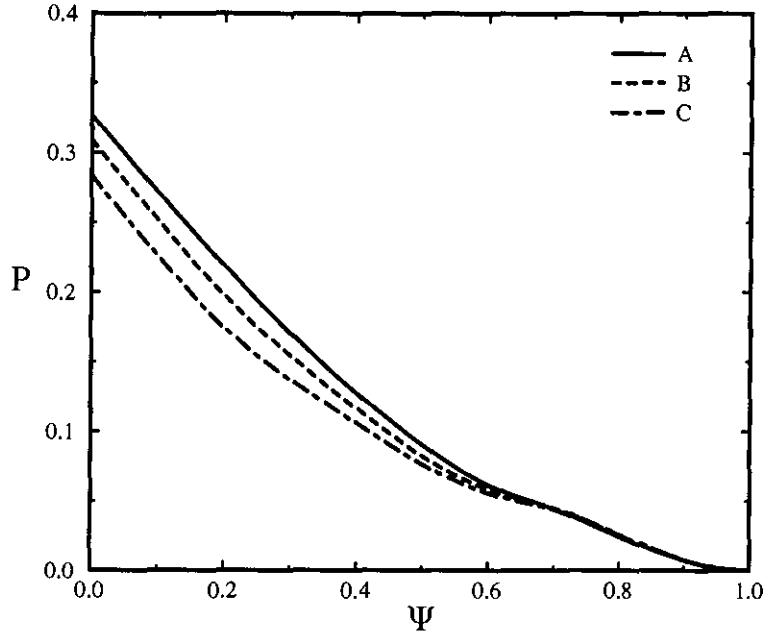
0.4
0.3
0.2
0.1
0.0
P
0.0
0.2
0.4
0.6
0.8
1.0
Ψ
A
B
C

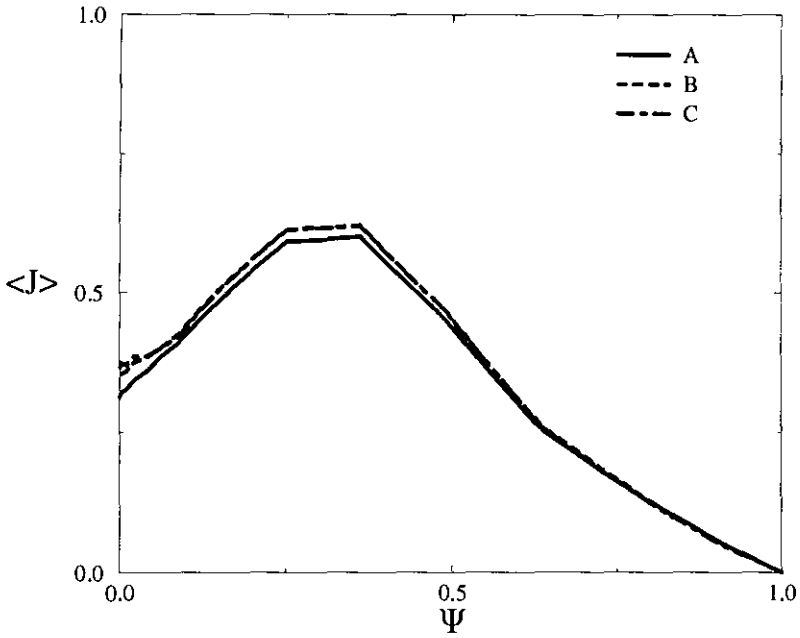
1.0
0.5
0.0
<J>
0.0
0.5
1.0
Ψ
A
B
C

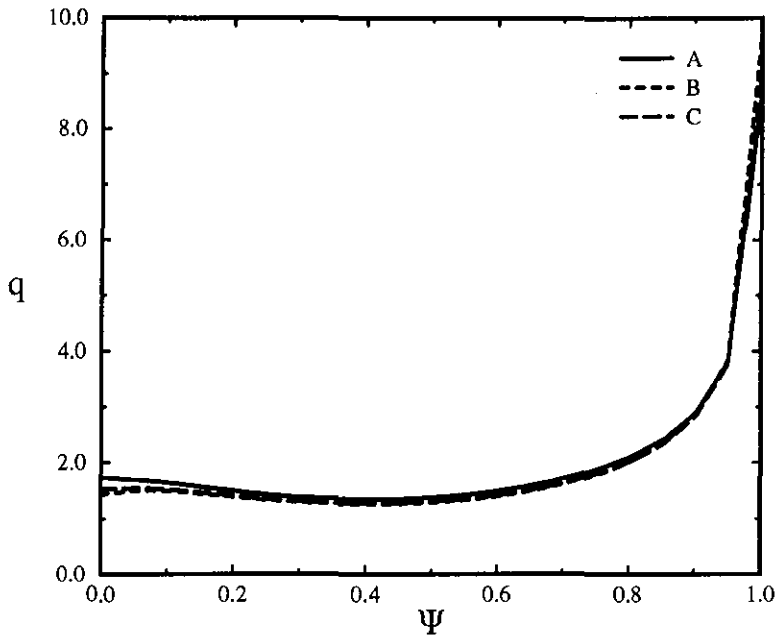

Figure 2.3: The pressure P (top left), averaged current density $< J >$ (bottom left), and the safety factor q vs. ψ for the equilibria A, B, and C.

$\bar{I}$	β_p	β_t	β_N
1.00	3.15	4.37	4.35
1.62	1.73	6.25	3.85
1.88	1.55	7.51	3.99

Table 2.3: Optimized critical ballooning betas for three different values of the normalized plasma current.

beta value as a function of the plasma current. The profiles Γ and Π are the same as those of equilibrium C and they are kept fixed. Results are shown in Figs. 2.4–2.6. For convenience, the actual current for the KSTAR tokamak and not the normalized current is plotted in these figures. The calcutions in this section were carried out with 129 poloidal grid points and 81 radial grid points.

In Fig. 2.4 the ellipticity is varied, in Fig. 2.5 the triangularity is varied, and in Fig. 2.6 the inverse aspect ratio is varied. The latter variation is not a variation of shaping. However, it is included here since it is a geometrical variation like the shaping ones.

When we focus on the plots of β_t in Figs. 2.4–2.6, it is clear that all the graphs have similar forms. First, their is a phase where β_t growths approximately linearly with I. Second, their is a sudden sharp decrease in β_t. The current at which this second phase sets in depends on the the specific values of the ellipticity, triangularity, and the inverse aspect ratio. For fixed plasma current in the first phase, increasing the ellipticity decreases the toroidal and normalized betas. An increase of the triangularity increases these betas whereas an increase of the inverse aspect ratio decreases them.

For constant aspect ratio, the maximum value of $\beta_t \approx 6.0$ is obtained for a plasma current around 2 MA. This is no coincidence, of course, since we started with profiles that were optimized for a plasma current of 2 MA and $\kappa = 2.0$, $\delta = 0.8$, and $\epsilon = 0.278$. For $\epsilon = 0.333$, however, the maximum $\beta_t \approx 6.4$ at $\bar{I} \approx 2.4$ MA.

The two phases visible in the β_t plots are also visible in the β_N plots. The parts of the graphs where β_N increases slightly with increasing plasma current correspond with the first phases, i.e., with the parts of the graph of β_t versus I where there is approximately a linear dependence. In this phase there is a clear dependence on the varied parameter (κ, δ, or ϵ). The second phase where β_N decreases rapidly shows less dependence on the varied variable. This is especially evident in the normalized beta plot in Fig. 2.5 where the triangularity is varied. The curves overlap greatly.

Note that for high triangularity and small ellipticity high values of the normalized beta, $\beta_N > 5$ can be achieved for low plasma currents. For optimized equilibrium profiles one would even get higher values.

It also follows from the normalized beta plots in Figs. 2.4 and 2.5, and in a

somewhat less convincing way from Fig. 2.6, that

$$\beta_{\mathrm{N}} \leq a - bI,$$

where a and b are constants with respect to the varied parameter: κ, δ, or ϵ. The specific values, however, depend on the values of the fixed parameters. For Fig. 2.4: $a = 7.3$, $b = 1.65$, for Fig. 2.5: $a = 7.1$, $b = 1.65$, and for Fig. 2.6: $a = 6.2$, $b = 1.2$. This is the same as saying that the curves β_{t} for the different values of the ellipticity in Fig. 2.4 (or the triangularity or inverse aspect ratio in Figs. 2.5 and 2.6) are enveloped by a parabola:

$$\beta_{\mathrm{t}} \leq aI - bI^2.$$

(a)

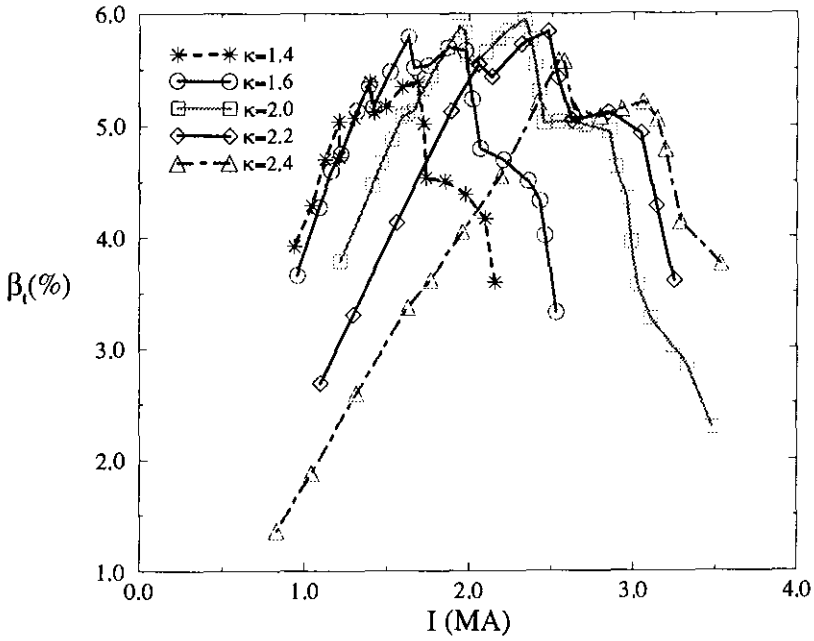
κ=1.4
κ=1.6
κ=2.0
κ=2.2
κ=2.4
β_t(%)
I (MA)
6.0
5.0
4.0
3.0
2.0
1.0
0.0
1.0
2.0
3.0
4.0

(b)

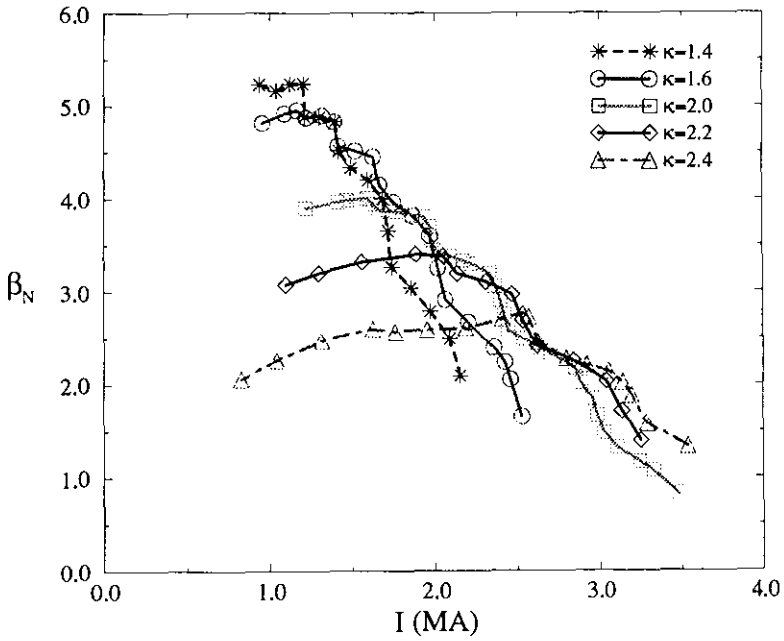
κ=1.4
κ=1.6
κ=2.0
κ=2.2
κ=2.4
β_N
I (MA)
6.0
5.0
4.0
3.0
2.0
1.0
0.0
0.0
1.0
2.0
3.0
4.0

(c)

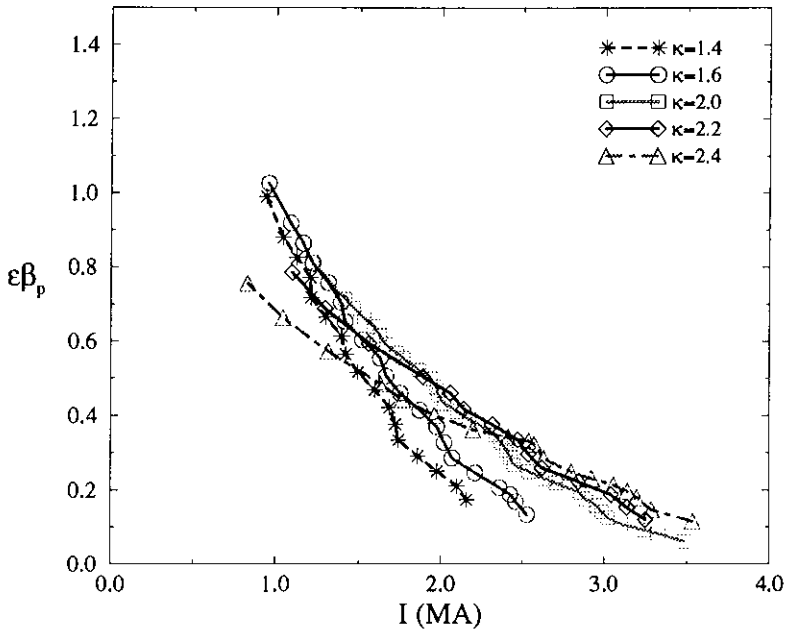

Figure 2.4: (a) Critical toroidal beta β_t, (b) critical normalized toroidal beta β_N, and (c) critical value of $\epsilon\beta_p$ as a function of the plasma current I for various values of the ellipticity κ. The triangularity and the inverse aspect ratio were fixed: $\delta = 0.8$ and $\epsilon = 0.278$.

(a)

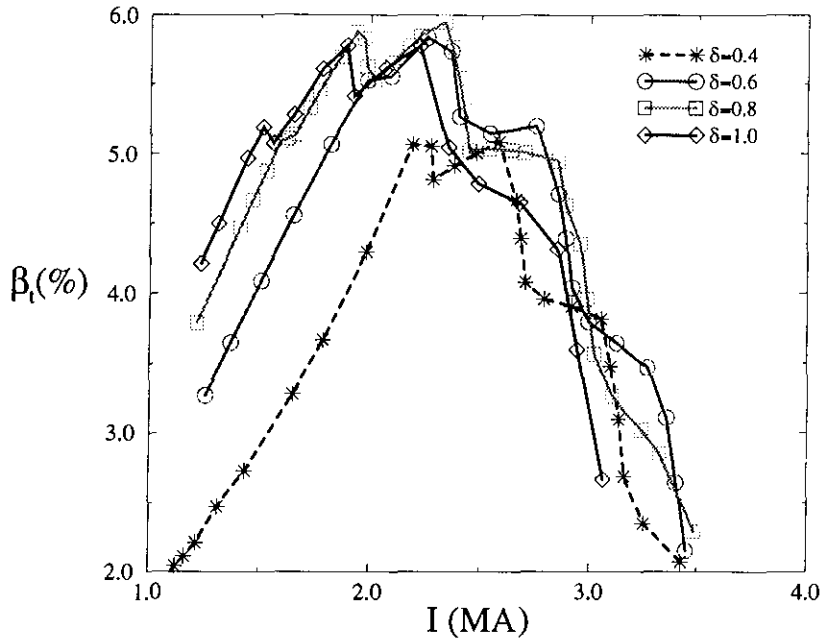
6.0
5.0
4.0
3.0
2.0
β_t(%)
1.0
2.0
3.0
4.0
I (MA)
δ=0.4
δ=0.6
δ=0.8
δ=1.0

(b)

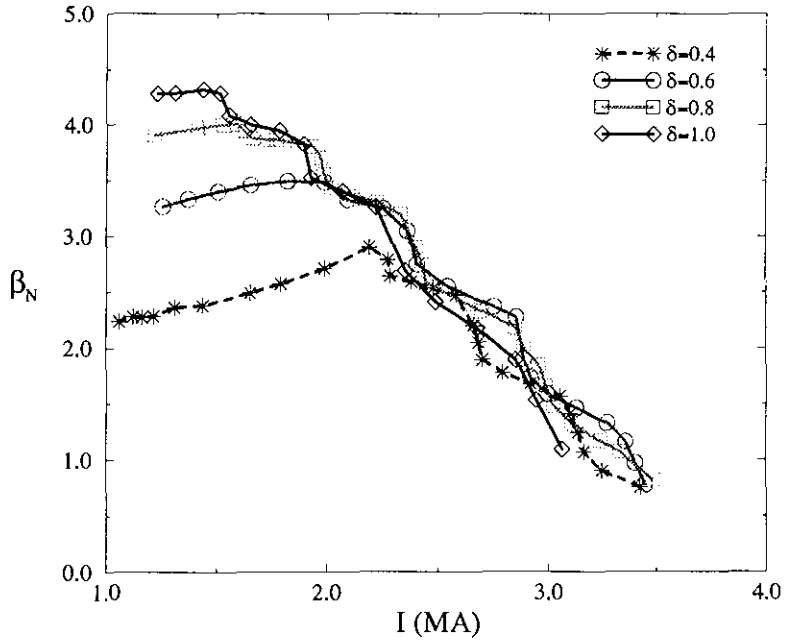
5.0
4.0
3.0
2.0
1.0
0.0
β_N
1.0
2.0
3.0
4.0
I (MA)
δ=0.4
δ=0.6
δ=0.8
δ=1.0

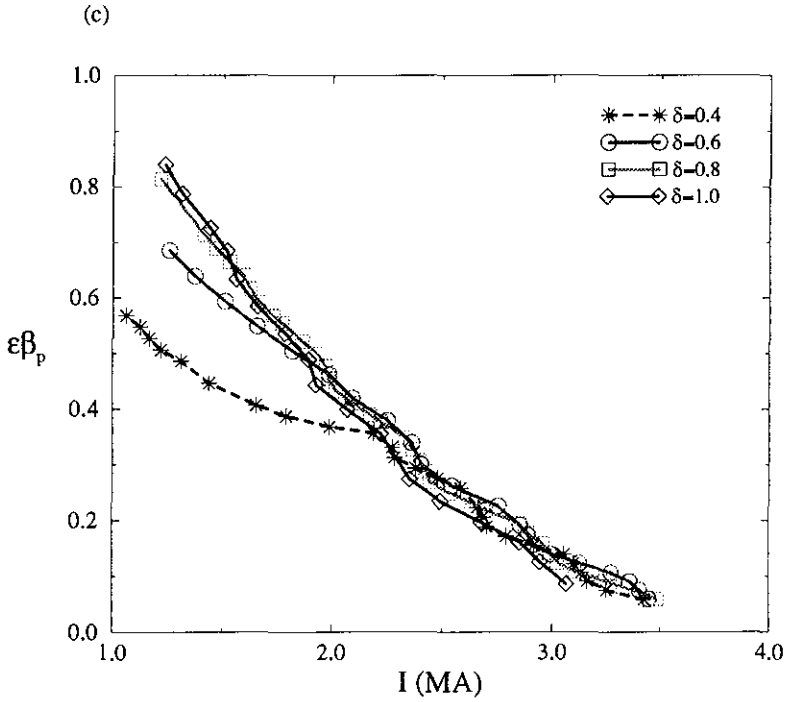

Figure 2.5: (a) Critical toroidal beta β_t, (b) critical normalized toroidal beta β_N, and (c) critical value of $\epsilon\beta_p$ as a function of the plasma current I for various values of the triangularity δ. The ellipticity and the inverse aspect ratio were fixed: $\kappa = 2.0$ and $\epsilon = 0.278$.

(a)

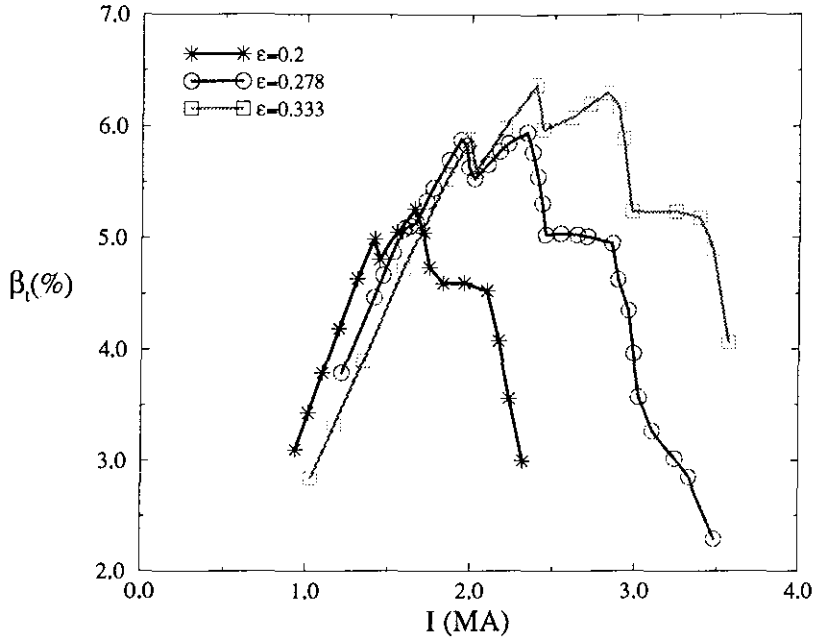
7.0
6.0
5.0
4.0
3.0
2.0
β_t(%)
0.0
1.0
2.0
3.0
4.0
I (MA)
ε=0.2
ε=0.278
ε=0.333

(b)

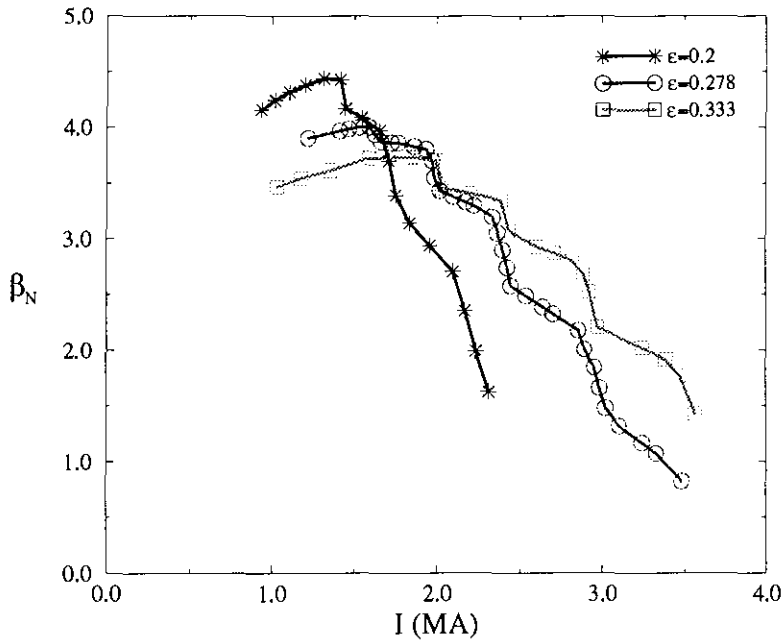
5.0
4.0
3.0
2.0
1.0
0.0
β_N
0.0
1.0
2.0
3.0
4.0
I (MA)
ε=0.2
ε=0.278
ε=0.333

(c)

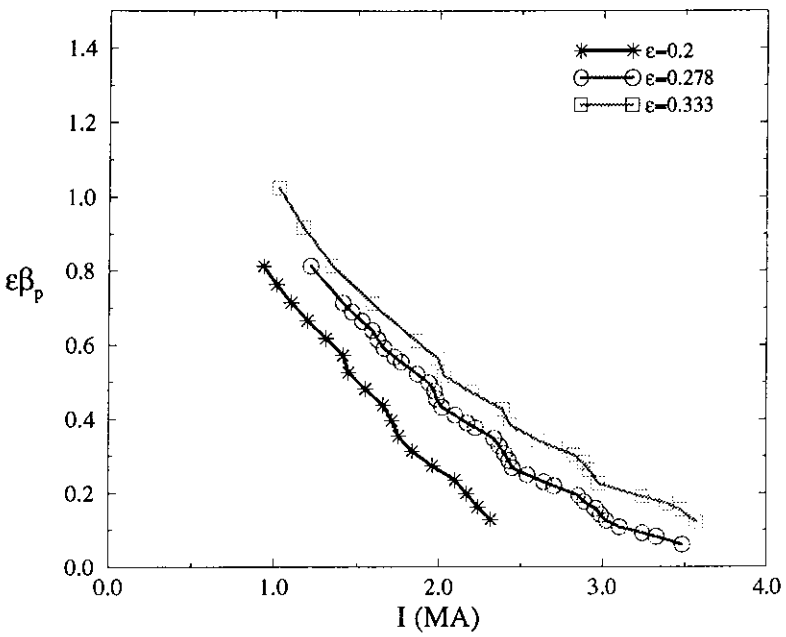

Figure 2.6: (a) Critical toroidal beta β_t, (b) critical normalized toroidal beta β_N, and (c) critical value of $\epsilon\beta_p$ as a function of the normalized plasma current for various values of the inverse aspect ratio ϵ. The ellipticity and the triangularity were fixed: $\kappa = 2.0$ and $\delta = 0.8$.

Chapter 3

Low-n stability analysis

3.1 Introduction

This chapter describes the low-n stability analysis of the marginal ballooning stable equilibrium B shown in section 2.3 (Fig. 2.3).

First, we discuss the convergence properties of the numerically computed growth rates in section 3.2. In section 3.3, we study the internal and external ideal instabilities. Both the effect of the poloidal beta and the position of an ideal conducting wall are presented. Resistive instabilities and the effect of resistivity on external instabilities are investigated in section 3.4. Finally, in section 3.5 we discuss the effect of the shape of the plasma.

3.2 Convergence properties of calculated low-n instabilities

Low-n instabilities are investigated with the spectral MHD code CASTOR [9, 12]. Convergence studies with respect to both the number of radial grid points and the number of Fourier harmonics are necessary since the KSTAR plasma cross-section is far from circular so that a lot of harmonics are required to get an accurate estimate of the growth rates. Furthermore, since a lot of rational q-surfaces are located in the plasma when inverted shear equilibria are considered (in general q_1 is large) a high radial resolution and a large number of Fourier harmonics are required to resolve the structure of the eigenfunctions on these surfaces well.

In Fig. 3.1 we show the convergence of the growth rate γ as a function of the number of Fourier harmonics M for a typical $n = -1$ instability found at $q_{\text{min}} = 1.99$. Here and in all next figures, the growth rate is normalized to τ_{A}^{-1}. From Fig. 3.1 it becomes clear that more than 21 harmonics are necessary to make a reliable extrapolation of the growth rate for $M^{-2} \to 0$. However, for instabilities with smaller growth rates, especially when one enters a stability window, we have often found that convergence is not as smooth as in Fig. 3.1 and that many more harmonics as well as radial grid points are needed to make an accurate extrapolation of the

growth rate. It also turns out that the equilibrium should be calculated with enough resolution since this improves the convergence of the growth rate considerably. This is shown in Fig. 3.2.

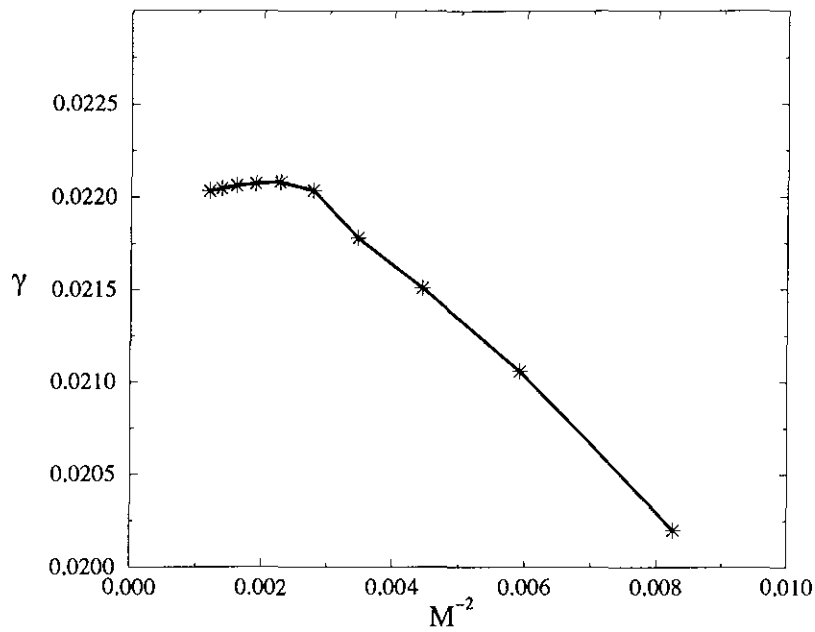

Figure 3.1: Typical convergence behavior of the growth rate of a low-n instability with the number of Fourier harmonics M that is used in the CASTOR stability code for a highly elongated and triangular cross-section plasma like KSTAR. The number of radial grid points used in the calculations of the growth rate was 101.

3.3 Ideal instabilities

Previous work on infernal modes [10, 7] revealed that the occurrence of infernal instabilities sensitively depends on the value of $nq_{\min}$, where n is the toroidal mode number of the perturbation and $q_{\min}$ is the minimum in the q-profile. Infernal instabilities only occur if $q_{\min}$ lies just below a rational q-value. These instabilities are driven by the pressure gradient and they can be stabilized by shear.

For the ballooning stable equilibrium B computed in section 2.3, a large region of low shear around $q_{\min}$ is present so that infernal modes may be present. However, the pressure gradient is also very small so that these modes may be suppressed.

3.3.1 Internal modes

Since $q_{\min}$ plays such a crucial role in determining stability with respect to infernal modes, a scan has been made of the ideal growth rate versus $q_{\min}$ for different values

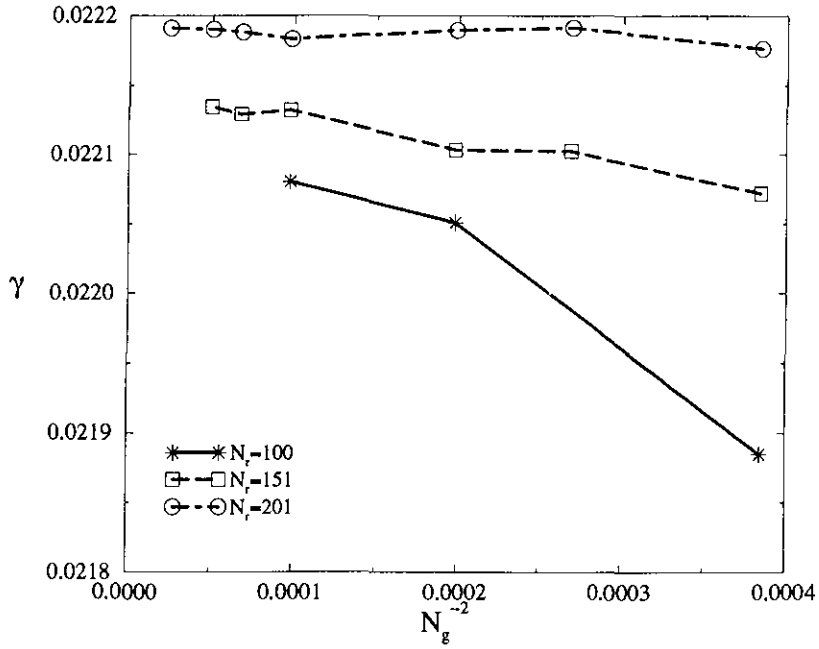

Figure 3.2: Convergence behavior of the growth rate of a low-n instability with the number of radial grid points used in the CASTOR stability code for a highly elongated and triangular cross-section plasma like KSTAR. The number of Fourier harmonics used in the calculations is $M = 21$. Three separate curves are shown representing the same instability but calculated using HELENA equilibria that were computed with 100, 151, and 201 radial grid points, respectively. All three equilibria were calculated with 129 poloidal grid points.

of the poloidal beta, β_p. In Fig. 3.3, q_{min} was varied through the safety factor on-axis q_0. Increasing q_0 increases q_{min}, but decreases the total plasma current I_p. The poloidal beta, β_p, was varied through the HELENA input parameter B. Furthermore, we put an ideally conducting wall on the plasma. The calculations were done using 101 radial grid points and 25 Fourier harmonics in CASTOR. For the instabilities around $q_{min} = 1.0$, we decreased the number of radial grid points to 51.

Fig. 3.3 reveals that the plasma is stable against ideal internal $n = -1$ instabilities for β_p slightly below 1.77 and $q_{min} > 1.23$, i.e., $I_p < 2.10$ MA. This shows that these modes do not give a more severe limit on the poloidal beta than the high-n ballooning modes. The ballooning modes are stable for $\beta_p < 1.77$ and $q_{min} > 1.27$, i.e., $I_p < 2.04$ MA (see table 2.1).

The radial mode structures of the instabilities for $\beta_p = 1.10$, $q_{min} = 1.06$ and for $\beta_p = 2.13$, $q_{min} = 2.03$ are shown in figure 3.4. These instabilities appear to be the $m/n = 1/1$ and $m/n = 2/1$ internal kink, respectively. The $m/n = 2/1$ internal kink is stable for β_p just below 1.77. However, the instability at $q_{min} = 1.0$ is difficult to stabilize by decreasing β_p. Like in the stability analysis of the KT-2

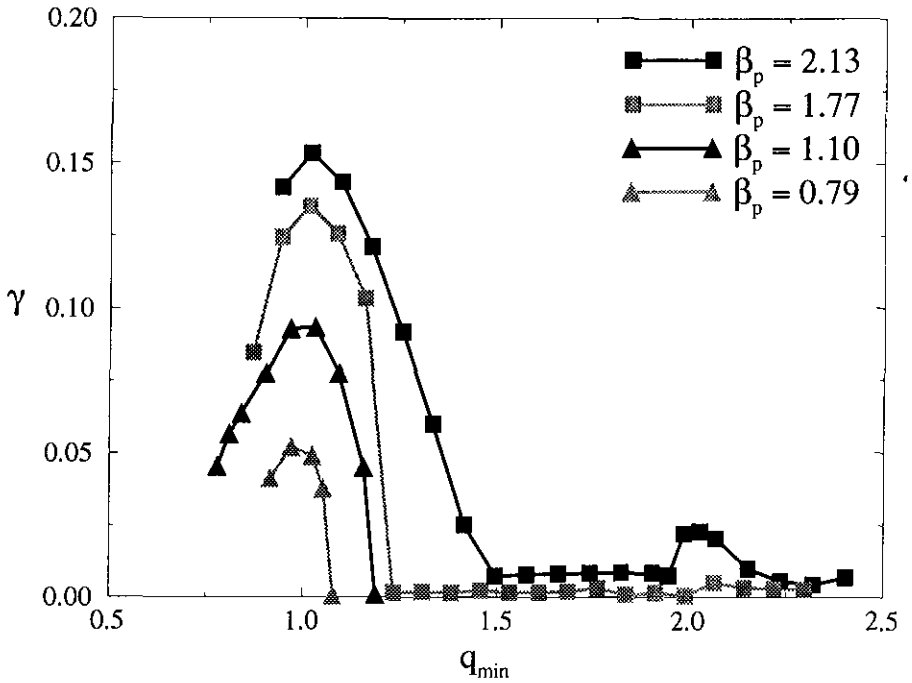

Figure 3.3: Growth rates of the largest $n = -1$ ideal instability versus $q_{\min}$ for different values of β_p. The wall put on the plasma. The scan over $q_{\min}$ is obtained by scaling the equilibrium through q on axis, q_0.

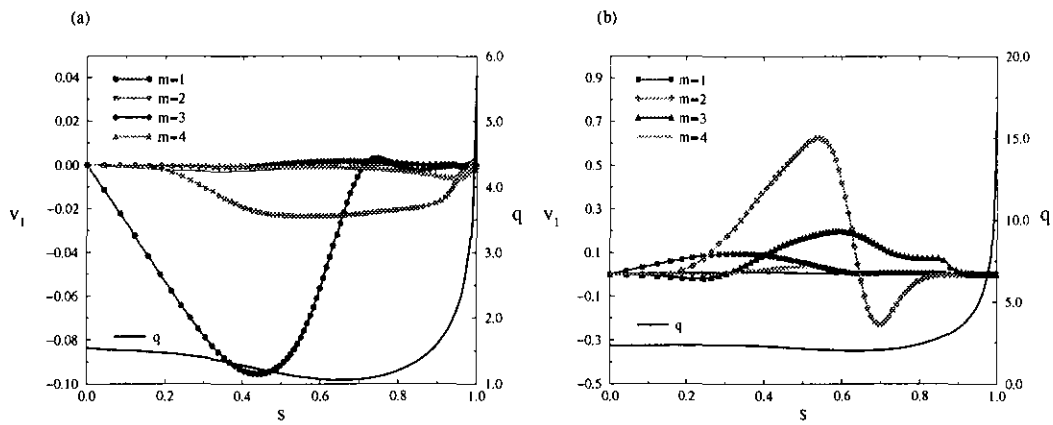

Figure 3.4: (a) Mode structure of the ideal internal instability at $\beta_p = 1.10$, $q_0 = 1.55$, and $q_{\min} = 1.06$ (cf. Fig. 3.3). (b) Mode structure of the ideal internal instability at $\beta_p = 2.13$, $q_0 = 2.35$, and $q_{\min} = 2.03$ in Fig. 3.3. For both modes, the largest Fourier harmonics of the velocity component normal to the flux surfaces, $v_1 \sim \xi \cdot \nabla\psi$ are plotted versus $s = \sqrt{\psi}$. The safety factor profile is also shown.

tokamak [11], no infernal instabilities were found. At least, they do not limit the maximum obtainable poloidal beta.

3.3.2 External modes

In Fig. 3.5, we have plotted the two largest growth rates, γ_1 and γ_2, versus the safety factor on the plasma edge, q_1, for three different positions of the ideal conducting wall r_w (normalized to the minor plasma radius). The poloidal beta is fixed at 1.10. The growth rates are calculated using 101 radial grid points and 25 Fourier harmonics and the vacuum is solved using 101 grid points and 25 harmonics. Furthermore, the ideally conducting wall has the same shape as the last closed flux surface.

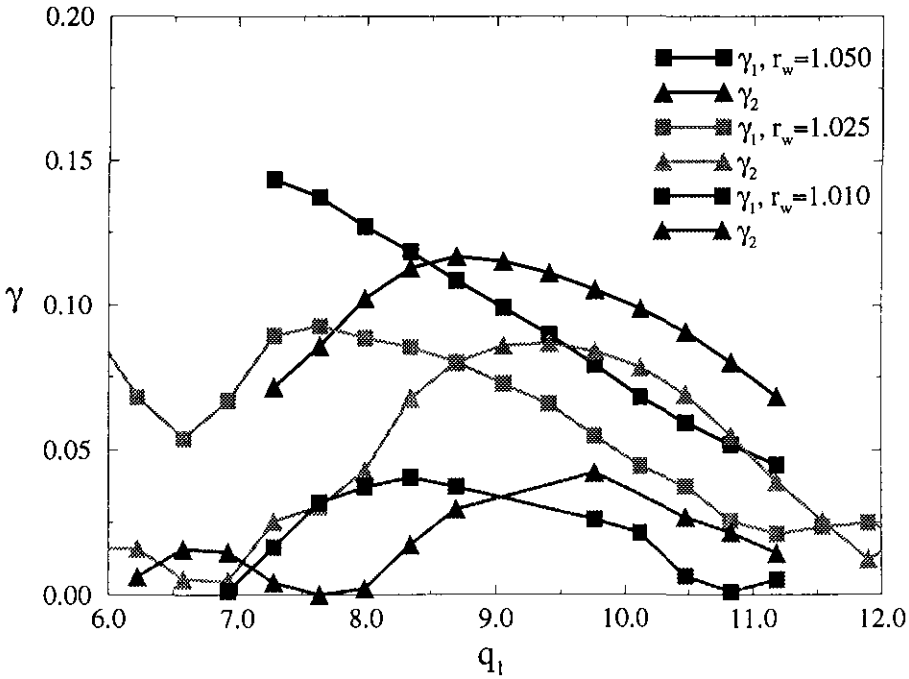

Figure 3.5: Growth rate of the two largest $n = -1$ ideal instabilities versus q_1 for three different values of the poloidal beta. This scan over q_1 is obtained by scaling the equilibrium through q_0. The poloidal beta is fixed at 1.10.

The growth rates are huge and these external instabilities can only be made stable by bringing the wall below 1% of the minor plasma radius. For $q_1 = 9.41$ and $r_w = 1.025$, the radial mode structure of γ_2 is shown in figure 3.6. This mode is localized at the plasma-vacuum interface in the region of high shear. The most dominant m-modes are the ones corresponding to the highest two rational q-surfaces located within the plasma.

In Fig. 3.7, the effect of poloidal beta on the two largest growth rates γ_1 and γ_2

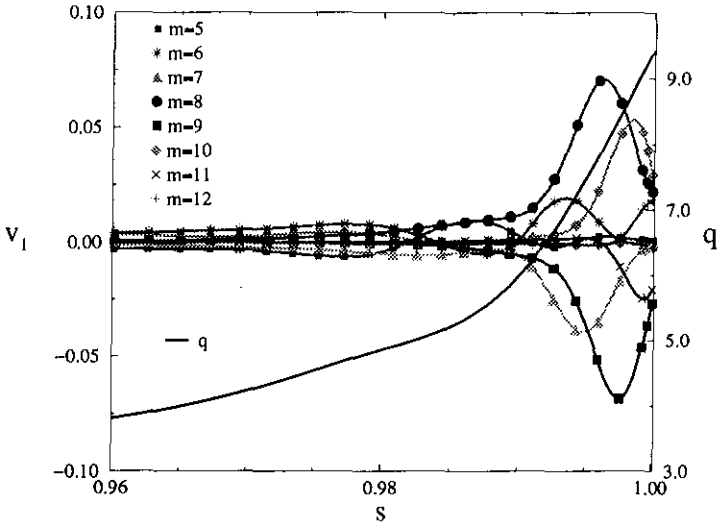

Figure 3.6: Mode structure near the plasma edge of the most unstable external instability, γ_2, at $q_1 = 9.41$, where $r_w = 1.025$, $\beta_p = 1.10$ (cf. Fig. 3.5). The largest Fourier harmonics of the velocity component normal to the flux surfaces are plotted versus $s = \sqrt{\psi}$. The safety factor profile is also shown.

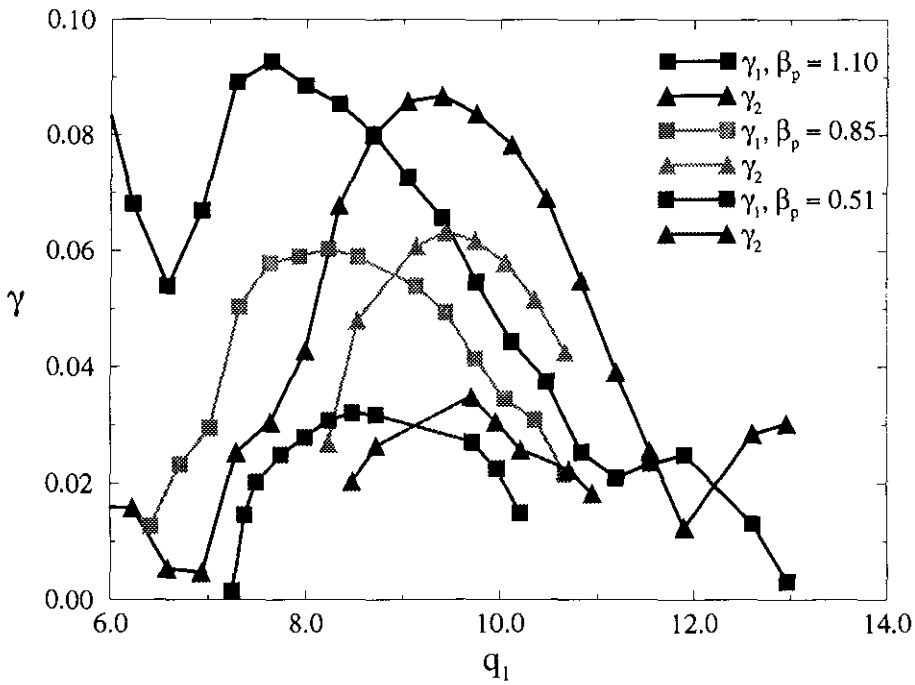

Figure 3.7: Growth rates of the two largest $n = -1$ ideal instabilities versus q_1 for three different values of the poloidal beta ($r_w = 1.025$).

versus q_1 are shown. The wall is fixed at $r_w = 1.025$. The number of grid points and Fourier harmonics that are used is the same as in Fig. 3.5. Decreasing the poloidal beta lowers the growth rates, but even for $\beta_p = 0.51$ they are still considerable as is the width of the unstable q_1-window.

3.4 Resistive instabilities

Fig. 3.8 shows the effect of the resistivity, η, on the growth rates of the two largest external instabilities for $q_1 = 9.41$, $\beta_p = 1.095$, and $r_w = 1.025$ (cf. figure 3.5). Here, the resistivity is normalised such that it is the inverse of the magnetic Reynolds number. This figure shows that the growth rates decrease with increasing resistivity. A possible explanation is a broadening of the perturbation because of the resistivity. Therefore, a wall stabilization is possible.

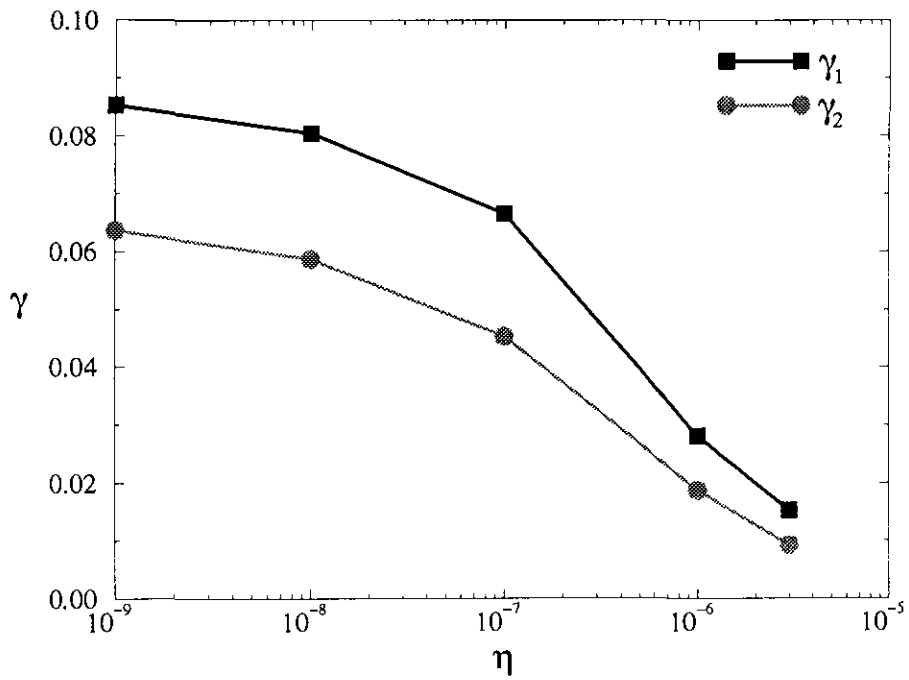

Figure 3.8: Growth rates of the two largest edge localized external modes as a function of the resistivity η at $q_1 = 9.41$, $\beta_p = 1.095$, and $r_w = 1.025$.

In Fig. 3.9, we have plotted the three most unstable resistive internal instabilities for $\beta_p = 1.095$, $q_0 = 2.8$, $q_{min} = 1.87$, and $r_w = 1.0$. Both γ_1 and γ_2 in figure 3.9 scale as $\eta^{\frac{1}{3}}$ indicating the interchange character of these modes [2]. For $\eta = 10^{-6}$ the radial mode structure of these resistive interchange instabilities is shown in Fig. 3.10. The double mode resonant $m = 2$ behaviour around the $q = 2$ surfaces is clearly

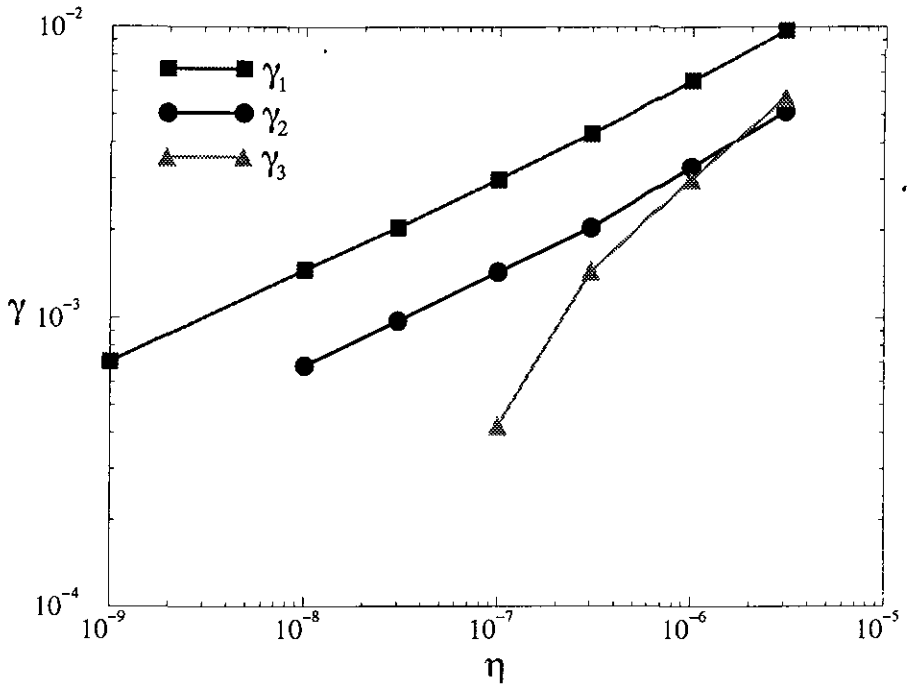

Figure 3.9: Growth rates of the three largest resistive internal modes as a function of the resistivity η for $q_0 = 2.8$, $q_{\min} = 1.87$, $\beta_p = 1.095$, and $r_w = 1.0$. Both γ_1 and γ_2 scale as $\eta^{\frac{1}{3}}$ indicating the interchange character of these modes. For $\eta = 10^{-6}$ the mode structure of γ_1 and γ_2 is plotted in Fig. 3.10.

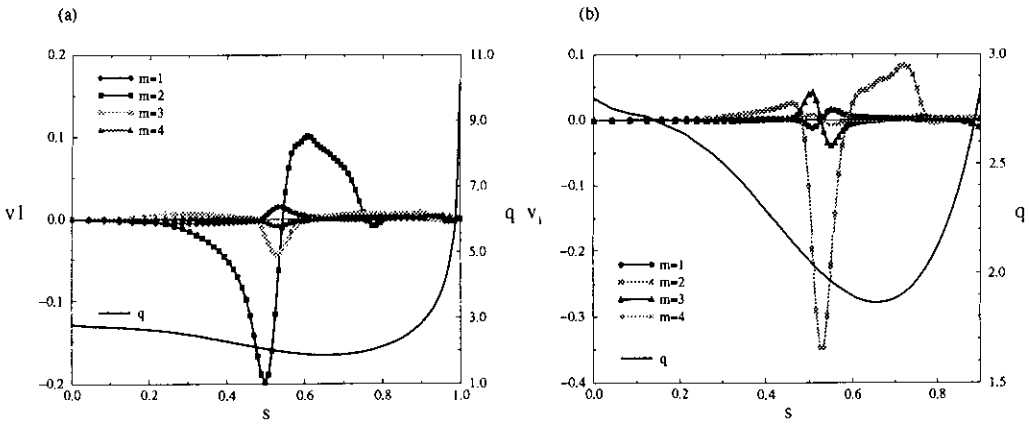

Figure 3.10: Mode structure of the two most unstable internal resistive instabilities for (a) γ_1 and (b) γ_2 of Fig. 3.9 for $\eta = 10^{-6}$. For both modes, the largest Fourier harmonics of the velocity component normal to the flux surfaces are plotted versus $s = \sqrt{\psi}$. The safety factor profile is also shown.

visible. Hence, for the considered equilibrium, these double resistive interchange modes are more important than the double tearing mode. Comparing Fig. 3.8 and 3.9, one notes that the growth rate of the internal modes become dominant over the external ones for $\eta > 10^{-6}$.

3.5 Shaping effects

The effect of the plasma shape, i.e., the dependence of the growth rate on the triangularity and elongation, also has been investigated. This was done by varying one of these parameters while keeping the other input parameters fixed.

Increasing the triangularity results in a higher average shear near the edge, i.e., a higher value of $q_1 - q_{\min}$, and in a higher poloidal beta. Figure 3.11 shows the effect of the triangularity on the growth rate of the ideal $n = -1$ instability plotted versus q_1, while keeping the elongation fixed at 2.0. Furthermore, we fixed the wall at $r_w = 1.025$. This figure shows that the growth rate increases with higher triangularity, but the width of the unstable q_1-window does not change significantly.

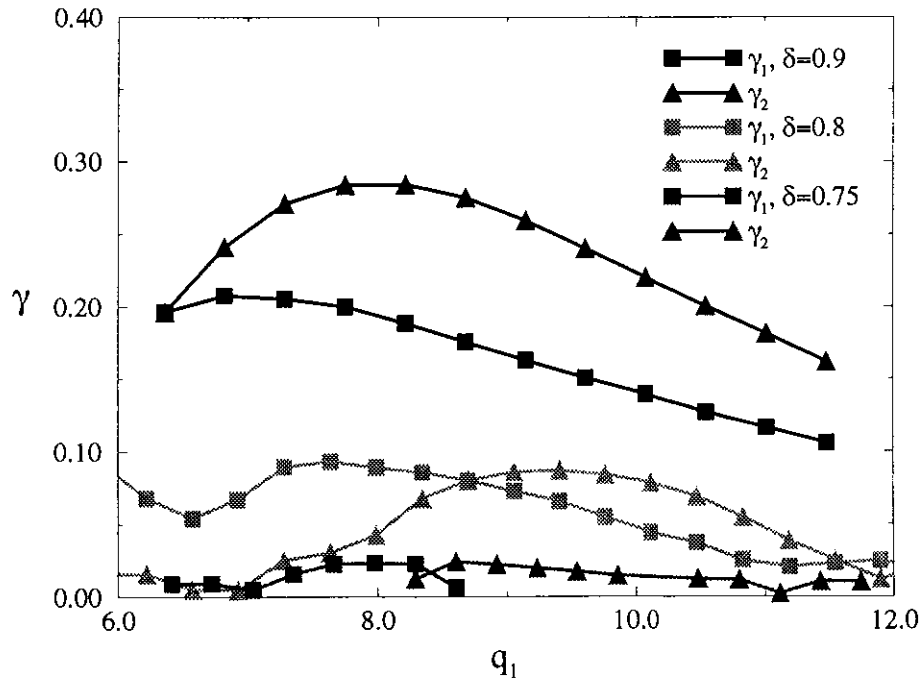

Figure 3.11: Growth rate of the two largest $n = -1$ instabilities versus q_1 for three different values of the triangularity δ. The wall position $r_w = 1.025$, the elongation $\kappa = 2.0$, and the HELENA input parameter $B = 2.0$. This corresponds to $\beta_p = 1.107$ for $\delta = 0.9$, $\beta_p = 1.095$ for $\delta = 0.8$, and $\beta_p = 1.090$ for $\delta = 0.75$.

Figure 3.12 shows the effect of the elongation on the growth rate of the ideal external $n = -1$ instability, while keeping the triangularity fixed at 0.8. Again, the wall was fixed at $r_w = 1.025$. Like in the case of the triangularity, increasing the elongation results in a higher average shear near the edge. But now the poloidal beta decreases. As can be seen in Fig. 3.12, the growth rate increases with increasing elongation, but again the width of the unstable q_1-window does not change significantly.

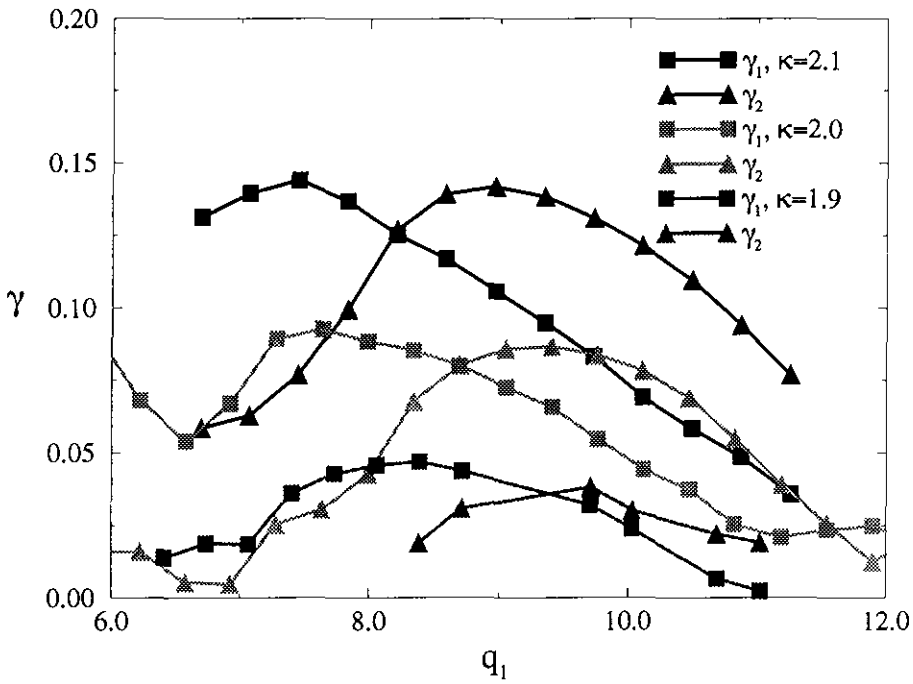

Figure 3.12: Growth rate of the two largest $n = -1$ instabilities versus q_1 for three different values of the elongation κ. The wall position $r_w = 1.025$, the triangularity $\delta = 2.0$, and the HELENA input parameter $B = 2.0$. This corresponds to $\beta_p = 1.075$ for $\kappa = 2.1$, $\beta_p = 1.095$ for $\kappa = 0.8$, and $\beta_p = 1.115$ for $\kappa = 1.9$.

Chapter 4

Conclusions

In this report, the MHD stability analysis of the KSTAR tokamak is described. The analysis was performed by means of the equilibrium code HELENA, the low-n resistive MHD code CASTOR, and a new high-n ballooning stability code BSE. Since the KSTAR tokamak is intended to operate with a large non-inductively driven bootstrap current, we have studied equilibria with inverted q-profiles.

For the ballooning study, we have used a typical averaged current density and pressure profile as obtained by the JETTO transport code in the modeling phase of profile control experiments. For the considered KSTAR geometry these profiles give rise to a q-profile characterized by high shear at the plasma edge. A ballooning optimization has been performed on the pressure profile. The equilibrium obtained is stable up to $\beta_p = 1.8$ and $\beta_t = 6.3\%$ for a total plasma current of 2.04 MA.

It has been shown that the $n = 1$ ideal internal modes do not set a more severe limit on the poloidal beta. Since we exploit the ballooning optimized profiles which are characterized by low pressure gradients in the region of low positive shear, no infernal instabilities are found.

The external modes limit the achievable poloidal beta considerably. They can only be stabilized by bringing an ideal conducting wall very close to the plasma edge. Typically, the distance of the wall to the plasma edge should be below 1% of the minor plasma radius. Furthermore, the growth rate of these modes decreases with increasing resistivity and decreasing poloidal beta. In addition to these external modes, we have found resistive internal instabilities. A detailed analysis of the mode structure and the scaling of the growth rate with the resistivity shows that these modes appear to be double resistive interchange instabilities. We have investigated the effect of shaping on the external instabilities. The growth rate of these instabilities increases with increasing triangularity and elongation.

Finally, the current profile obtained by the JETTO transport code appearsto have a slightly too large current gradient at the edge of the plasma for stability of the KSTAR tokamak. Therefore, external modes with huge growth rates are found. Consequently, this kind of current profile should be avoided. A forthcoming paper will consider equilibria with lower current gradients at the edge.

Appendix A

Ballooning stability code BSE, user guide version 1.3

BSE (Ballooning Stable Equilibria) is a FORTRAN 90 program that determines whether or not an equilibrium constructed with HELENA [8, 13] is ballooning stable. It makes use of PPPLIB (Plasma Physics Plotting LIBrary), HGOLIB (Hans GOedbloed LIBrary), and spline.o from the CASTOR code [9, 12]. The BSE program should be compiled with the command:

```
f90 -o bse bse.f90 spline.o ppplib.a hgolib.a
```

A.1 Input files

BSE uses NAMELIST formatting to read in data from the input file '*input*'. Three namelists are defined, viz. `PARS`, `PROF`, and `QPAR`. The parameters in namelist `PARS` determine the extended polodial interval, the resolution, and the ψ-interval that is considered for the ballooning σ-stability test. The parameters in namelist `PROF` determine how the equilibrium is defined in HELENA [13]. Finally, namelist `QPAR` consists of q_0 and α that can be used for rescaling the toroidal current [5].

Namelist PARS

`TO`	value ϑ_0 for ballooning modes that are localized around ϑ_0, see Eq. (2.11);
`DBT, DBF`	truncated range of the extended poloidal variable for the Suydam method;
`DBT`	mesh size $\Delta\vartheta$ for the Suydam method;
`SIGMA`	cut-off for the growth rate in the criterion for σ-stability;

MHARM — number of harmonics to be used to interpolate from the domain $0 < \vartheta < 2\pi$ to the extended domain;

PSI_START, PSI_END — The range of flux surfaces to scan for ballooning stability (must be integer values).

Namelist PROF

A — HELENA ouput parameter [13] which is an eigenvalue of the Grad-Shafranov equation;

B — HELENA input parameter determining the amplitude of the pressure profile;

IGAM — HELENA switch parameter determining whether the profile $\Gamma(\psi)$ or $F(\psi)F'(\psi)$ is used and how this profile is specified:

1 – $\Gamma(\psi)$ given as a 8th order polymonial with coefficients AGA, BGA, ... , HGA, i.e., $\Gamma(\psi) = 1 + a_\gamma\psi + \cdots + h_\gamma\psi^8$,

2 – not implemented,

3 – not implemented,

4 – $\Gamma(s)$ read in via namelist input DF2 on an equidistant $s = \sqrt{\psi}$-mesh,

5 – $F(\psi)F'(\psi)$ given as a 8th order polymonial with coefficients AGA, BGA, ... , HGA, i.e., $F(\psi)F'(\psi) = 1 + a_\gamma\psi + \cdots + h_\gamma\psi^8$,

6 – not implemented,

7 – $F(s)F'(s)$ read in via namelist input DF2 on an equidistant $s = \sqrt{\psi}$-mesh,

8 – not implemented;

AGA–HGA — coefficients $a_\gamma, \ldots, h_\gamma$ of the 8th order polynamial $\Gamma(\psi)$ for the case IGAM = 1, and of $F(\psi)F'(\psi)$ for the case IGAM = 5;

IPAI — HELENA switch parameter determining how the profile $\Pi(\psi)$ is specified (analogous to IGAM):

1 – $\Pi(\psi)$ given as a 8th order polymonial with coefficients API, BPI, ... , HPI, i.e., $\Pi(\psi) = 1 + a_\pi\psi + \cdots + h_\pi\psi^8$,

2 – not implemented,

3 – not implemented,

4 – as IPAI = 1,

5 – as IPAI = 1,

6 – $P'(s)$ read in via namelist input DPR on an equidistant $s = \sqrt{\psi}$-mesh,

7 – not implemented;

API–HPI coefficients $a_\pi, \ldots, h_\pi$ of the 8th order polynamial $\Pi(\psi)$ for the case IGAM = 1, 4, and 5;

NPTS number of points on which the input profiles DF2 (IGAM = 4 and 7) and DPR (IPAI = 7) are given;

DF2 array of dimension NPTS on an equidistant mesh $s = \sqrt{\psi}$ defining the input profile for $\Gamma(s)$ in the case IGAM = 4, and for $F(s)F'(s)$ in the case IGAM = 7;

DPR array of dimension NPTS on an equidistant mesh $s = \sqrt{\psi}$ defining the input profile for $P'(s)$ in the case IPAI = 7.

Namelist QPAR

QO_HELENA HELENA value of the safety factor on axis (q_0);

QO_START, QO_END range of q_0-values to scan;

NQO number of q_0-values;

ALFA HELENA input parameter α.

A.2 Mapping file

BSE needs a mapping file to read in the equilibrium. This file is created by HELENA [13], and must be copied to the BSE home directory as file '*mapping*'.

A.3 Output

The BSE output is generated on the standard output. The printed list contains for every value q_0 of the q_0 scan the following information:

- the new values of q_0, $q_{\min}$, q_1, and the new HELENA α;
- the flux-surface number IS that is evaluated;
- the corresponding ψ-value;
- the value of $-D_{\mathrm{I}}$, where $-D_{\mathrm{I}} > 0$ is the Mercier criterion;
- 'ballooning stable' or 'unstable', and, in case of instability, the value of ϑ where α becomes negative.

A.4 A remark on using BSE

For profile optimization, we recommend that HELENA should be used without mesh accumulation since the input profiles DPR and DF2 are defined on an equidistant mesh in $s = \sqrt{\psi}$.

Bibliography

[1] J.W. Connor, R.J. Hastie, and J.B. Taylor, *Shear, periodicity, and plasma ballooning modes*, Phys. Rev. Lett. **40**, 396–399 (1978).

[2] H.P. Furth, J. Killeen, and M.N. Rosenbluth, *Finite resistive instabilities of a sheet pinch*, Phys. Fluids **6**, 459 (1963).

[3] R.M.O. Galvão and J. Rem, *Application of the Suydam method to the ballooning stability problem*, Comp. Phys. Comm. **22**, 399–402 (1981).

[4] J.P. Goedbloed, *Lecture Notes on Ideal Magnetohydrodynamics*, Rijnhuizen Report 83-145 (1983).

[5] ———, *Some remarks on computing axisymmetric equilibria*, Comp. Phys. Comm. **31**, 123–135 (1984).

[6] ———, *Toroidal theory of MHD instabilities*, Transactions of Fusion Technology **29**, 121–132 (1996).

[7] H.A. Holties, G.T.A. Huysmans, J.P. Goedbloed, W. Kerner, V.V. Parail, and F.X. Söldner, *Stability of infernal and ballooning modes in advanced tokamak scenarios*, Nucl. Fusion **36**, 973–986 (1996).

[8] G.T.A. Huysmans, J.P. Goedbloed, and W. Kerner, *Isoparametric bicubic Hermite elements for solution of the Grad-Shafranov equation*, Proc. CP90 Conf. on Comp. Phys. Proc., World Scientific Publ. Co., 1991, p. 371.

[9] ———, *Free boundary resistive modes in tokamaks*, Phys. Fluids **B5**, 1545 (1993).

[10] J. Manickam, N. Pomphrey, and A.M.M. Todd, *Ideal MHD stability property of pressure driven modes in low shear tokamaks*, Nucl. Fusion **27**, 1461–1472 (1987).

[11] S. Poedts, A. de Ploey, and J.P. Goedbloed, *MHD stability analysis of the KT-2 tokamak plasma*, Rijnhuizen Report 96-227 (1996).

[12] S. Poedts, H.A. Holties, J.P. Goedbloed, G.T.A Huysmans, and W. Kerner, *CASTOR: Installation and User Guide*, Rijnhuizen Report 96-229 (1996).

[13] S. Poedts, H.A. Holties, J.P. Goedbloed, G.T.A. Huysmans, and W. Kerner, *HELENA: Installation and User Guide*, Rijnhuizen Report 96-228 (1996).

[14] B.R. Suydam, *Direct numerical solution of the variational problem arising from stability theory*, Culham Report (1968).

[15] A. Sykes, M.F. Turner, and S. Patel, *Beta limits in tokamaks due to high-n ballooning modes*, Controlled Fusion and Plasma Physics (Aachen, W. Germany), vol. II, 11th European Conference, 1983, pp. 363–366.